Case Studies in Construction Materials 21 (2024) e03457

Contents lists available at ScienceDirect

Case Studies in Construction Materials

journal homepage: www.elsevier.com/locate/cscm

Case study

Compressive performance and damage mechanism of concrete short columns confined by steel wires reinforced 3DPM

Chang Sun [a], Jiawang Li [a], Qiong Liu [a,*], Kailun Chen [b], Wengui Li [b], Feng Pan [c]

[a] School of Environment and Architecture, University of Shanghai for Science and Technology, Shanghai 200093, PR China
[b] Centre for Infrastructure Engineering and Safety, School of Civil and Environmental Engineering, The University of New South Wales, NSW 2052, Australia
[c] Shanghai Construction Industry Fifth Construction Group Co., Ltd., Shanghai 200063, PR China

ARTICLE INFO

Keywords:
3D printed mortar (3DPM)
Steel wire reinforced
Compressive performance
Damage mechanism
Analytical model

ABSTRACT

The incorporation of steel reinforcement in cast concrete can effectively enhance the ductility and strength of the concrete. In this paper, the steel wires reinforced 3D printed mortar (3DPM) was utilized as the external restraint for two series of short concrete columns (S-series: square section, C-series: circular section). Three different wire diameters (fine, medium, and thick) were considered as experimental variables. The experimental results indicate that the specimens reinforced with medium steel wires in both series exhibited strengths comparable to or superior to those of the unreinforced specimens. In terms of crack control, the specimens with the appropriate reinforcement ratio exhibited excellent performance, showing the smallest crack widths for both C-M and S-M specimens. It is found that in both S and C series that an appropriate reinforcement ratio positively influences the load-bearing capacity of the restrained columns. Furthermore, a calculated model for the uniaxial compression model of ECC confined concrete was proposed. The findings reveal that the calculated model is conservative and effective in predicting the compressive strength of the short column, with the exception of the C-F specimen.

1. Introduction

The application of 3D printing in civil engineering is a highly promising area of development. Some 3D printed buildings are already being used for practical purposes. Compared to the traditional method of pouring concrete, 3D printing can be faster, more cost-effective, and can reduce carbon emissions [1,2]. The use of 3D printing not only saves money but also helps to reduce carbon emissions. Additionally, 3D printing can reduce the need for formwork and eliminate the time required for formwork erection, thus accelerating the project [3]. 3D printing is an emerging technology with promising applications in the field of civil engineering. The utilization of 3D printing in real projects necessitates careful consideration of material selection for concrete, printing requirements, and operational performance. Therefore, it is essential to study the fundamental requirements and development trends of 3D printing in the field of civil engineering.

Despite the evident value of 3D printing in numerous engineering applications, it is crucial to consider the potential degradation of mechanical properties in 3D printed materials due to the limited strength of the interlayer bonding surface during the printing process [4]. In current research, numerous scholars have employed various methods to study the comprehensive performance of 3DPM,

* Corresponding author.
E-mail address: lq612@usst.edu.cn (Q. Liu).

https://doi.org/10.1016/j.cscm.2024.e03457
Received 3 March 2024; Received in revised form 15 June 2024; Accepted 24 June 2024
Available online 28 June 2024

Nomenclature

f_l	circumferential pressure of the concrete
$f_{l,3DP}$	perimeter pressure provided by 3DPM
$f_{l,sw}$	perimeter pressure provided by helical steel wire
$\sigma_{h,3DP}$	circumferential tensile stress of the 3DPM
$\sigma h,s\omega$	circumferential tensile stress of the wire
k_h	effective constraint coefficient in the horizontal direction
k_v	effective constraint coefficient in the vertical direction
B	side length
Dt	effective diameter printing thickness
rA	radius of the fillet cross-sectional area
s	net vertical spacing between the transverse wires
A_{sw}	cross-sectional area of wire
ε_u	tensile strain corresponding to the tensile strength of the wire
ε_{sw}	tensile strain of the wire
f_y	yield strength of the steel wire
f_{cc}	peak axial stress at constant circumferential pressure
ε_{cc}	compressive strain at constant circumferential pressure
F	the load applied to the confined concrete column
ε_l	circumferential tensile strain at the concrete surface
A_{3DP}	cross-sectional area of the outer concrete layer
f_{cr}	tensile stress when the tension-to-compression stress ratio is 0.25
ε_{cr}	tensile strain corresponding to the uniaxial model
ε'_{cr}	tensile strain corresponding to biaxial model
μ	poisson ratio of the 3DPM, taken as 0.17
E_{3DP}	elasticity modulus of 3DPM
E_C	elasticity modulus of concrete
σ_{3DP}	axial compressive stress of 3DPM
σ_c	axial compressive stress of concrete
ε_s	the ultimate axial strain of the confined concrete column
ε_c	axial compressive strain of 3DPM
f_{ce}	the cubic compressive strength of 3DPM
σ_{ce}	axial compressive strength of 3DPM, taken as $0.9f_{ce}$
ε_{ce}	axial compressive strain of 3DPM, taken as 0.005
ε_e	equivalent annular tensile strain
ε_h	circumferential tensile strain of the concrete surface
ε_θ	hoop tensile strain of 3DPM
r_a	inner diameters of the printed paste
$r_b\gamma$	outer diameters of the printed paste constant factor
f_{co}	compressive stress under peak axial stress of unconfined concrete
ε_{co}	compressive strain under peak axial stress of unconfined concrete
A_c	cross-sectional area of the inner concrete layer

focusing on enhancing mechanical properties and durability through different processes and materials. It was found that the process parameters of printing, including print speed, layer height, time interval, and geometry of the printed layer affect the strength of the component [5,6]. The cross-sectional geometry of the component can affect the stability of the print and the failure mode [7]. In addition incorporating fibers or wrapping steel tubes in the printed material can improve the mechanical properties [8]. A significant number of researchers have discovered that incorporating cementitious composite materials and fibers can enhance the load-bearing capacity and deformation resistance of 3DPM [9–11]. The enhancement of the mechanical properties of 3DPM represents a significant research focus within the field of 3D printing materials. Once effective improvements have been made, the promotion of this material is likely to be widespread. Consequently, the study of different reinforcement methods to enhance the performance of 3D printed components is likely to have considerable application potential.

In addition to researching material properties and process parameters, it is worthwhile to investigate the conversion of plain 3D printed components into reinforced 3D printed components. Implanting the traditional steel frame in 3D printed components may not only disrupt the printed material and cause collapse but also affect the construction process of 3D printing [12,13]. Insertion of reinforcement bars during the printing process is a key direction of current research [14].Some scholars used square hoops with pre-drilled reinforcement holes [15] and a built-in hoop formwork method [16] to insert the reinforcement inside the bond structure, resulting in a 78.2 % increase in the strength of 3D printed components. Other scholars have investigated how to automate the printing

process to improve the mechanical properties [17,18]. Li et al. [19] investigated the continuous steel cable reinforcement method and found that the moment carrying capacity and bond strength of the reinforcement increased by 263 % and 71 %, respectively, compared to plain concrete. Mechtcherine et al. [20] innovatively proposed a method of 3D printing of steel reinforcement bars using gas-shielded welding to improve the material properties. Therefore, the study of effective methods for incorporating reinforcement materials to improve the mechanical properties of 3D printed components is an important area of research.

In the research of 3D printed components, many scholars have found that, in addition to internal reinforcement, strengthening the external constraints of components is also an important method to enhance their mechanical performance, especially the compressive properties of columns [21]. It was found that high-strength transverse reinforcement could improve the post-peak ductility index of the restrained specimens, and reducing the transverse reinforcement spacing could further improve the ductility and maximum load of the constructs [22]. In addition carbon fibre [23] and glass fibre [24] can also enhance the axial compressive properties as well as the axial deformation of the columns. Furthermore, it was found that after the use of FRP constrained 3D printed columns, the former exhibited higher axial stiffness and compressive capacity compared to normal cast columns due to the constraints imposed by the outer material on the deformation of the inner material [25]. Some other scholars have also found that outer restrained reinforced concrete columns can improve compressive performance. Among them, Yuan et al. [26] improved the compressive strength of the specimens by 38.5 per cent by using FRP dense die-cast concrete columns. Xiong et al. [27] has found that improving the bonding effect between the materials can enhance the overall constraint. Fibers and expanders can effectively improve the bond stiffness and bond strength of the FRP reinforcement, thereby strengthening the constraint effect. Zhao et al. [28] investigated the axial compressive properties and ductility of concrete reinforced with innovative wire mesh and modified high-strength mortar composites. Therefore, using 3DPM with reinforcing bars as an outer frame to restrain the inner concrete can enhance the compressive properties of the component.

According to the above research, taking into account the constraint effects of reinforcing 3D printing materials is of significant importance for enhancing its practical value in engineering applications. In this paper, high-strength steel wire is selected as the reinforced material, which is embedded in the 3DPM during the printing process to form different styles of 3DPM shells. At the same time, concrete with the same proportion is poured inside to form a constrained concrete short column. The damage process of the short concrete column, the restraining effect of steel wire confined 3DPM, and the force state of the mortar body are studied to obtain the stress-strain analysis model of uniaxial compression of concrete short column confined by steel wire reinforced 3DPM.

2. Experimental methods

2.1. Raw materials

Table 1 shows the mix proportion of 3DPM used in this experiment, which used Portland ordinary cement (P·O 42.5) and river sand as the fine aggregate. The water-cement ratio of 3DPM was 0.26. The addition of silica fume to the mix can improve the viscosity between the mixed materials, and increase the compressive properties and durability of the 3DPM [22]. Nano clay was used to improve the viscosity of the 3DPM, and hydroxypropyl methylcellulose (HPMC) could improve the compatibility of the 3DPM. The defoamers could reduce the air bubbles generated by HPMC during mixing to improve the density of the 3DPM, sodium gluconate (SG) slowed the setting time of the 3DPM, and SP was a polycarboxylic acid water reducer [29,30].

2.2. Preparation of steel wire-embedded printing

Fig. 1 shows the sample preparation process of this test. The printing system used in this test is the CABR-3DPRT mortar 3D printing system manufactured by Construction Research and Measuring Instrument Co. To control the variables of the test, the fluidity of 3DPM in this test is 180 mm. The printing speed in this test is as follows: squeezing speed 2.5 rad/s, xy-direction moving speed 50 mm/s, z-direction speed 10 mm/s. The internal part of the printing motor is modified to embed the steel wires into the mortar during the printing process. A stepper motor was added in the upper end of the machine, so that the steel wire uniform speed through the motor and the steel tube, and finally embedded in the 3DPM inside. The material of the steel wire used in this study is consistent, with varying diameters of steel wire. Specifically, the steel wire diameters are 0.5 mm for fine steel wire, 1.0 mm for medium steel wire, and 1.5 mm for thick steel wire.

Two series of short columns were tested in this experiment: short columns with a circular cross-section of 150×300 mm^2 (C-series) and short columns with a square cross-section of $150\times150\times300$ mm^3 (S-series). The C-series short columns are classified into four types based on the different steel wire diameters: specimens with no steel wires are defined as C-N, those with fine steel wires as C-F, those with medium steel wires as C-M, and those with thick steel wires as C-T. Similarly, S-series short columns have three types: specimens with no steel wires (S-N), specimens with fine steel wires (S-F), and medium steel wires (S-M). The steel wire follows the printing path embedded in the 3DPM interior. During the 3D printing process, it was found that the thick steel wire in the corner of the S-series specimen was exposed and could not be embedded in the 3DPM. Therefore, the S-T specimen is not considered in this study.

Table 1
Mixture proportion of mortar (unit: kg/m^3).

Mix	Cement	Sand	Silica fume	Nano-clay	HPMC	Defoamer	SG	SP	Mixing water
M1	1000	1000	230	5	1.28	1	0.7	1	260

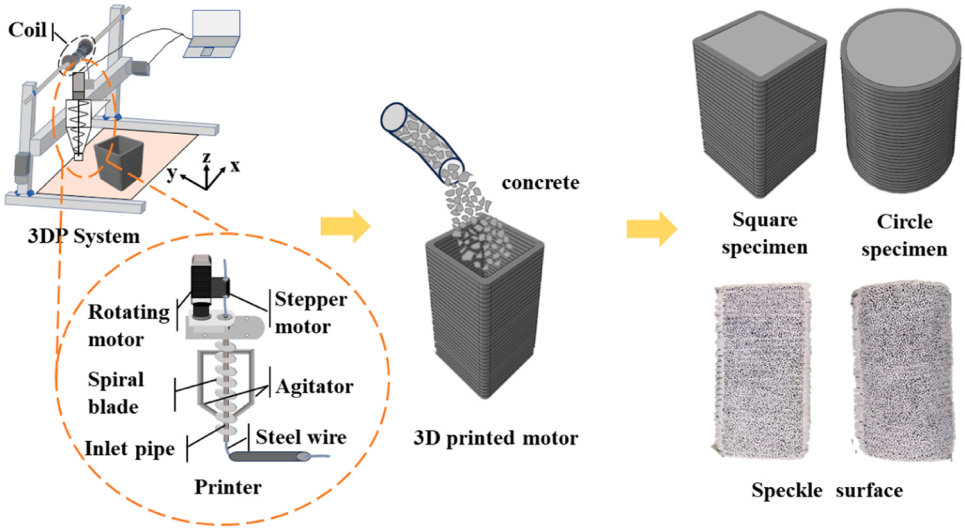

Fig. 1. Manufacturing process of short columns.

After 7 days following the 3DPM casting, the filled concrete was cast into the center to form short concrete columns. In addition to printing short columns, respectively, $100\times100\times100$ mm^3 cubes and $150\times150\times300$ mm^3 prisms with the same mixture proportions of 3DPM and filled concrete in short columns were cast. The mechanical properties of 3DPM, filled concrete, and steel wire are shown in Table 2.

After 28 days of standard curing, preparations before loading were made for the short columns. The upper and side surfaces of all specimens were polished to a smooth. For C series short columns, the semi-circular side was painted white, while for S series short columns, one side was painted white. After the white paint was set, irregular scattering spots with a diameter of approximately 2 millimeters, occupying around 14 pixels, were sprayed onto the white area.

2.3. Compressive strength test

Fig. 2 shows the loading device used in this test. The load recording for this test is provided by the loading machine and the axial displacement is provided by the displacement transducers (LVDT) at the front and rear. As the specimens in this test were 3DPM, the specimens showed a stack of layers with the unevenness of the top and bottom layers on the outer surface, and the 3D camera was used to facilitate the ability to recognize the change in concavity and convexity of the layers. In this test, the camera shooting frequency is 2 seconds each, and the average for each specimen is 150 shots. The loading rate of the test machine was 5 kN/s, and loading started after preparation was completed.

3D-DIC (Digital Image Correlation) was used to measure the crack propagation process and overall damage displacement during specimen damage, which refers to the use of a high-definition digital camera to capture specific surface deformations and other parameters [29]. In this technique, the digital camera captures and tracks the deformation of scattering points pre-sprayed on the specimens, and uses the change in grey scale values to obtain deformation data on the sample surface [31].

3. Results and discussion

3.1. Stress-strain curves

After loading, the compression stress-strain curves for two series specimens are shown in Fig. 3. For the calculation, the loading surface area of S-series specimens was 225 mm^2, and the value of C-series specimens was 177 mm^2.

Table 2
Mechanical properties of 3DPM, concrete, and steel wire.

	3DPM	Concrete	Fine steel wire	Medium steel wire	Thick steel wire
Diameter/mm	/	/	0.5	1.0	1.5
100 m/kg	/	/	0.10	0.39	1.56
Tensile capacity/(kN)	/	/	0.56	1.32	2.70
Compressive/Tensile strength/(MPa)	80	18	/	/	/
Modulus of elasticity/(GPa)	35.6	23.4	195	195	195

Note：100 m/kg means weight of 100 m steel wire.

Table 3
Parameters in the calculation process.

Specimen	ε_e	$r(mm)$	$\lvert\varepsilon_l\rvert$	$f_l(MPa)$
S-N	0.005	12.5	0.007	0.84
S-F				1.00
S-M				1.39
C-N	0.005	0	0.009	1.09
C-F				1.19
C-M				1.78
C-T				2.09

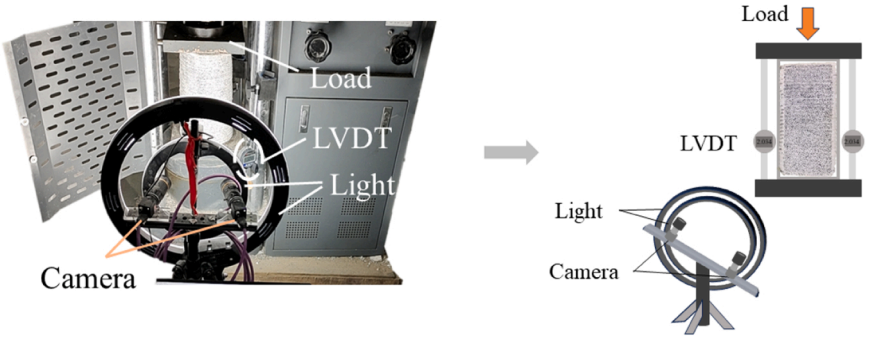

Fig. 2. Testing setup.

Fig. 3(a) shows the stress-strain curves of the specimens in S-series. The curves for specimens with different diameters of steel wires show similar trends. The curve can be divided into three stages. The first stage is a slow-rising stage, rising to around 4 MPa. The second stage is an approximately linear rising stage until the peak stress, with a noticeable increase in slope compared to the first stage. The third stage is an approximately linear descent stage. The peak stress of the S-N specimen is approximately 31 MPa. The addition of fine steel wires results in a reduction of about 19 % in the peak stress, while the addition of medium steel wires leads to an increase of about 33 %. The strain corresponding to peak stress for the three types of specimens is similar, around 0.008. Curves for specimens in C-series are shown in Fig. 3(b). The trend of the C-series specimen curves is the same as that of the S-series, which is also approximated to be divided into three stages. The peak stresses of the three specimens C-N, C-M, and C-T were approximated with values in the range of 34–37 MPa. Consistent with the S-series, the lowest stress was found in the specimen with fine steel wire. The peak stress of C-F decreased by about 27 % compared to the value of C-N The strain corresponding to the peak stress of four specimens in C-series was approximately 0.007.

When comparing the two types of specimens, it was found that for specimens without reinforcement, the compressive stress of C-N was 20 % higher than that of S-N. In the two series of specimens, the effect of steel wires on the ultimate compressive capacity was different. The addition of fine steel wires led to a decrease in the compressive stress of the specimens in both series. The medium steel

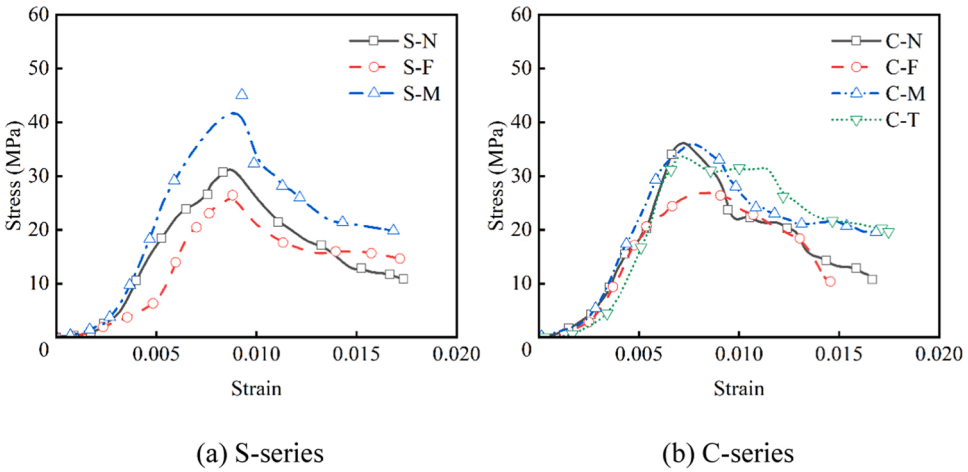

Fig. 3. Stress-strain curve of short column specimens.

wires in the S-series specimens play a role in increasing the compressive capacity. The effects of medium and thick steel wires on the compressive stress of the C-series specimens were not significant. There are two main reasons for the negative effect of fine steel wires on compressive stress. Firstly, the cross-sectional area of the steel wire is too small, which prevents it from fully utilizing its tensile capacity during the loading process. Secondly, the steel wire embedded in the mortar causes disturbance, reducing the bond between the mortar and the wire, resulting in a decrease in the stress.

The addition of steel wire has a certain beneficial effect on the residual stress after the peak load of the two series of specimens. Compared with specimens without reinforcement, a certain extent of decrease was observed on the slopes of the descending stage of the curves for specimens with steel wires. Overall, the stress-strain curves became smoother with the addition of fine steel wire, but the peak stresses decreased. After adding medium steel wire, the peak stress of the square specimen increased by 33 % and was the highest among all the columns at 41.8 MPa. After adding coarse steel wire, the peak stress of the round specimen changed little, but the ductility improved significantly. It can be concluded that properly configuring the diameter of the steel wires helps improve the restraint effect of 3DPM.

Furthermore, scholars have highlighted the significance of hoop spacing in enhancing the bearing capacity of confined concrete columns [32]. This experiment primarily focuses on the use of steel wire as hoop reinforcement in the 3D printing process to improve the load-bearing capacity of concrete columns. However, the spacing may deviate slightly due to the flow of mortar during the printing process, which may have a minor impact on the overall structure.

3.2. Destruction process and crack development

3.2.1. S-series destruction process

The crack width of specimens varied by different strain states over time and the distinct crack patterns in square and circular columns. Consequently, the strain states of each column at three load levels (60 %, 80 %, and 100 %) and its final damage morphology are illustrated in Fig. 4.

In Fig. 4(a), when the load reaches 60 % of ultimate stress, the primary crack in the S-N specimen extends from the top to the bottom, and a subtle strain concentration zone appears in the lower left corner. When the load reaches 80 % of the ultimate value, the

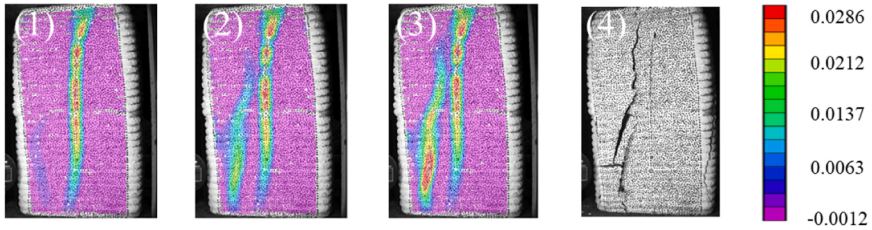

(a) S-N failure process and Exx nephogram

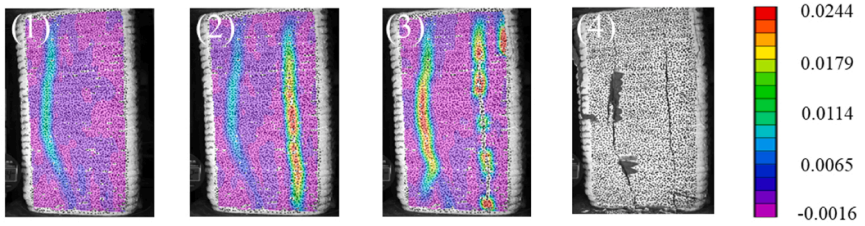

(b) S-F failure process and Exx nephogram

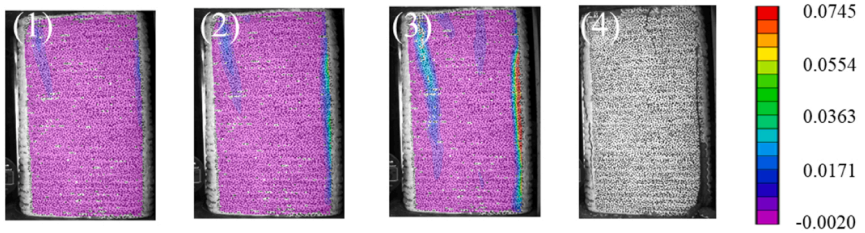

(c) S-M failure process and Exx nephogram

Fig. 4. Strain state of square specimens under (1) 60 %, (2) 80 %, (3) 100 % loading and (4) damage results.

strain near the main crack remains unchanged, while the strain value on the lower left zone significantly increases. When the load reaches the peak load, a secondary diagonal crack forms on the left side, reaching the same strain level as the main crack, while the 3DPM on the periphery begins to gradually peel off. When the load continues rising until the damage occurs, two cracks enlarge, and transverse cracks are produced at the intersection. Additionally, cracks have formed at the lower right corner of the specimen.

In Fig. 4(b), a subtle strain concentration zone occurs on the left side of S-F after the load reaches 60 %, the corresponding region eventually develops a through crack. After the load reaches 80 % of its capacity, a vertical crack forms on the right side of the specimen, where the strain is higher than on the left side. After reaching the peak load, the primary crack on the right side expanded rapidly, excessively wide cracks result in discontinuous strain distribution. The strain at the crack on the left side gradually increases until failure, leading to an increase in crack width accompanied by some mortar peeling off near the crack, and the steel wire has been pulled off.

In Fig. 4(c), a strain concentration zone appears in the upper left corner of S-M specimen when the load reaches 60 %. When the load reaches 80 %, a strip-shaped strain concentration zone appears along the right edge of the specimen, with values larger than those in the upper left corner. After reaching the peak load, the strain along the right edge of the specimen further increases. When the load continues to increase until failure, a nearly through vertical crack appears along the right edge of the specimen, with the 3DPM at the

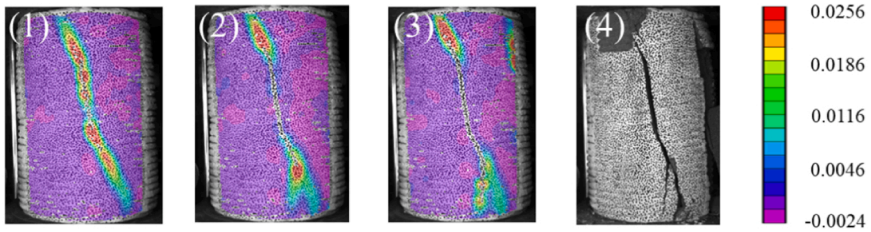

(a) C-N failure process and Exx nephogram

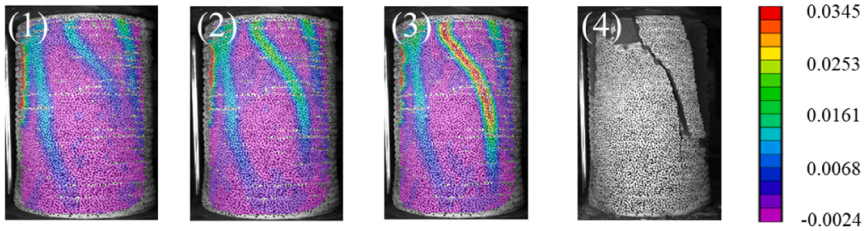

(b) C-F failure process and Exx nephogram

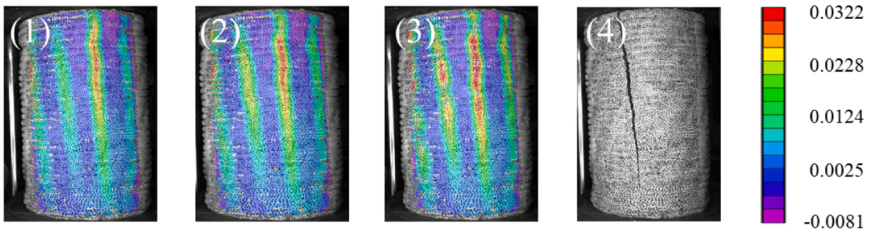

(c) C-M failure process and Exx nephogram

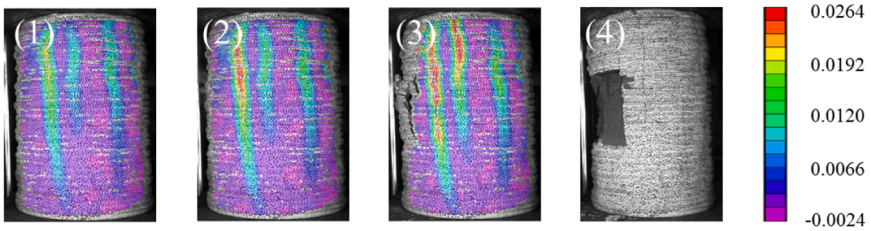

(d) C-T failure process and Exx nephogram

Fig. 5. Strain state of circular specimens under (1) 60 %, (2) 80 %, (3) 100 % loading and (4) damage results.

lower right corner peeling off. Additionally, some small cracks have appeared on the left side, and some of the steel wires at the upper end have been pulled off.

It can be observed that the cracks in the S-series specimen primarily originate at the top and extend downward. The strain distribution changes significantly as the cracks develop. When no reinforcement or fine steel wires were used, the specimens tended to show a greater number of cracks and a wider crack width. However, when medium steel wires were used, the number of cracks decreased, and the cracks became narrower. It is indicated that increasing the diameter of the steel wire is beneficial for enhancing the confinement capacity in S-series columns.

3.2.2. C-series destruction process

In Fig. 5(a), once the load reaches 60 % of its capacity, an incomplete crack can be seen from the upper left to the lower right in the C-N specimen, at an angle of approximately 30 degrees to the vertical direction. When the load reaches 80 % capacity, the central part of the main crack expands significantly, and the crack at the bottom splits into two downward-extending cracks. When the load reaches its peak level, the strain change in the main crack is minimal, and a strain concentration region appears at the upper right corner. After failure, it was observed that significant deformation occurred near the main crack, with large areas of mortar detachment observed at the starting point of the crack and the lower right.

In Fig. 5(b), after the load reaches 60 % of its capacity, four strain concentration zones are noticed at the top of C-F, with the highest strain observed at the leftmost edge. When the load reaches 80 % of its capacity, two strain concentration zones in the center gradually extend downward, and the strain increases slightly. When the load reaches its peak, the strain values in the strain concentration zone distributed from the middle of the upper part towards the lower right of the specimen show a significant increase, corresponding to a visible main crack after failure. Meanwhile, mortar detachment is observed above and below the main crack.

In Fig. 5(c), after the load reaches 60 % of its capacity, C-M exhibits four strain concentration zones from the top to the bottom, with the third one experiencing the highest strain. After the load reaches 80 % of its capacity, there is no significant change in the value of the strain. The strain at the location of the second strain concentration zone increased obviously after the load reached its peak value. When the specimen is damaged, it can be observed that the main crack develops downward along the second strain concentration location on the left side. At the same time, it was observed that the crack width on the surface of the C-M specimen was significantly finer than that in the C-N and C-F, and the degree of peeling of the 3DPM shell around the specimen was lighter.

In Fig. 5(d), after the load reaches 60 % of its capacity, three strain concentration zones appear in the C-T specimen, accompanied by a localized increase in stress at the upper right end. After the load reaches 80 % of its capacity, the strain at the leftmost strain concentration zone significantly increases. When the load reached its peak value, obvious cracks, and mortar detachment can be noticed in the middle of the left side of the specimen. After failure, The 3DPM shell completely peeled off from the left middle part, with the steel wire broken and the internal concrete exposed. Additionally, the fine cracks are visible at the middle position of the specimen. The circular specimen exhibits a high number of cracks during rupture, and these cracks are parallel to each other and intersect the bottom of the column obliquely. Compared with C-N, cracks in the specimens with steel wires appear later, and there are more and finer cracks inside the specimens before failure.

Based on the above damage changes of all 3D printed confined concrete short columns, it can be observed that the damage of the short columns initially originates from the micro-cracks formed in the outer layer of 3DPM. The square columns are particularly susceptible to developing cracks at the corners of the column ends. As the load increases, the cracks gradually widen and extend downward. The cracks in round columns are mostly diagonal, while square columns are characterized by vertical cracks at the corners of column ends and diagonal cracks on the plane. As the cracks gradually changed from vertical to oblique, the outer layer of mortar began to peel off. During the early spalling stage, the outer layer of the concrete primarily cracks due to the lateral pressure from the

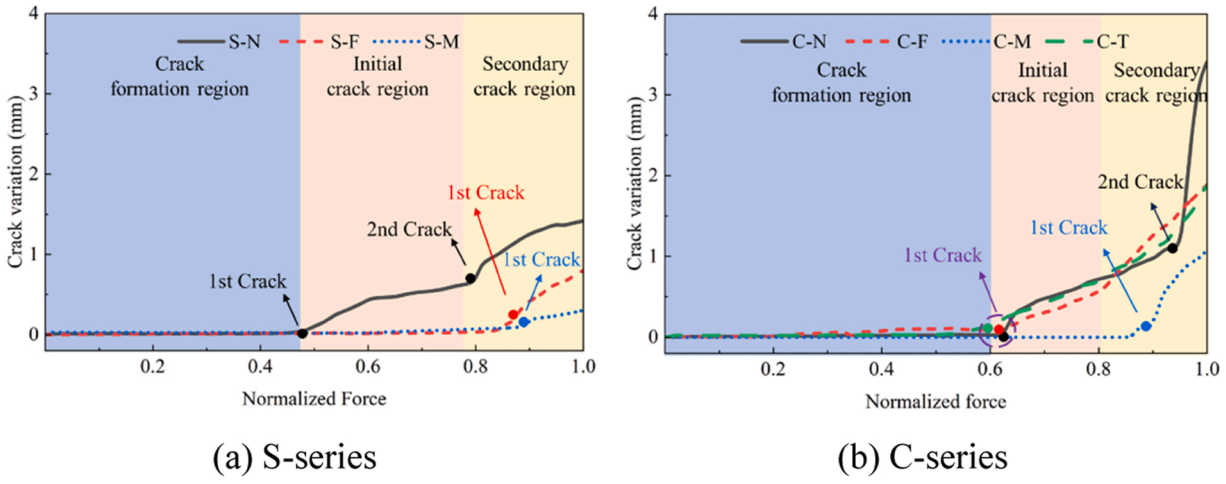

Fig. 6. Evolution of transverse cracking width.

internal expansion of the concrete. As stress gradually increases, lateral deformation intensifies, and the outer layer is constrained by the steel wire when it detaches. At this stage, the steel wire's restraint has not reached its limit, leading to incomplete spalling of the layer. After reaching the load limit, the outer mortar begins to shed over a large area, and both the 3DPM and the internal steel wire commonly fracture.

3.2.3. Crack development

Considering the potential impact of adding steel wire on the crack propagation of the specimen in various load sections, this paper employs Digital Image Correlation (DIC) to analyze the development of the crack on the positive surface of the specimen. It also generates the crack propagation process of the specimen under various load conditions, as shown below:

Fig. 6(a) illustrates the cracking width development process of S-series specimen. The transverse cracking width on the surface of the S-N specimen begins to expand when the load reaches almost 46 % of the peak load and then cracks rapidly expand further after reaching 80 % of the peak load. No visible cracks can be seen in the two specimens with steel wires of S-series until 88 % of the peak load. At peak load, the transverse cracking width of the specimen without steel wire was greatest, followed by the specimen with fine wire, and the lowest for the specimen with medium wire.

Fig. 6(b) illustrates the cracking width development in the C-series specimen. After the load reaches approximately 60 % of the peak load, the transverse cracking width begins to increase on the surface of the C-N, C-F, and C-T specimens. Subsequently, the cracks in the three specimens increased at almost the same rate. The cracking width in the specimens without steel wires (C-N) increased rapidly when the load reached 94 % of the peak load. The cracks in specimens with medium steel wires (C-M) appear the latest, and the cracking width is the finest.

The trend in transverse cracking width change for C-series specimens is similar to that for S-series specimens. It is noticed that the number of cracks and cracking width of C-series specimens are higher than those of S-series. On the other hand, incorporating steel wires with an appropriate reinforcement ratio reduces the rate of crack width increase and also decreases the crack width at rupture. This finding is supported by the observation that the cracking widths of both C-M and S-M are the lowest in both series. The appropriate reinforcement ratio can effectively enhance the load-bearing capacity of concrete columns.

4. Uniaxial compression model of concrete analysis

4.1. Compressive stress-strain models of confined concrete

The compressive properties of confined concrete have been extensively researched, leading to the development of various compressive stress-strain models for confined concrete. However, there are limited studies on mortar embedded with steel wires using the 3D printing process as a reinforcement material. This study uses high-strength stainless steel wire rope to reinforce engineered cementitious composites [32]. The stress-strain relationship of wire-embedded 3D-printed confined concrete will be derived in three steps: (1) determining the circumferential pressure of the outer 3D-printed mortar on the inner concrete; (2) defining the stress-strain relationship of the outer mortar under the complex stress state; and (3) determining the restraining effect of the wire-embedded reinforced 3D-printed mortar and defining the load-strain relationship of the concrete column. strain relationship.

4.2. Confining pressure

There are two types of cross sections of 3D printed concrete used in this experiment: circular cross sections (with a radius of 150 mm) and square cross sections (in which the four corners are rounded and the side length is 150 mm), as shown in Fig. 7. The outer layer consists of a 25 mm thick 3DPM with a steel wire ring embedded within it, while the inner layer is made of C20 poured concrete.

The analytical model of the cross-section constraint force is obtained based on the cross-section shape (as shown in Fig. 8(a)). The analytical model of the constraint force for a circular column cross-section can be based on the concrete intrinsic model adopted by Li et al. [33].

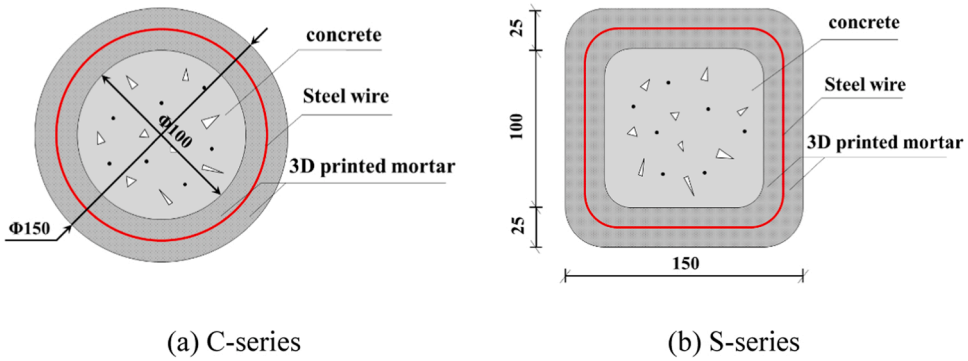

Fig. 7. Concrete column sections.

Unlike the uniform constraint forces in restrained circular columns, in restrained square-section concrete columns, the hoop stresses are nonuniform along the circumference of the concrete core section [34], which are larger at the four corners of the section and smaller at the straight edges. As shown in Fig. 8(b), the total cross-sectional area consists of the ineffective constraint area (IA) and the effective constraint area (EA). To simplify the constraint forces, an equivalent circular cross-section is used instead of a square cross-section, and the effective diameter (D) of the equivalent circular cross-section can be determined by the following equation [35]:

$$D = \sqrt{2}B \tag{1}$$

where B represents the side length of the square cross-section. Hence, the lateral strain and lateral circumferential pressure are equivalent to the circumferential strain and circumferential pressure, respectively. As shown in Fig. 9, the circumferential pressure of the center-cast concrete is provided by the 3DPM embedded with steel wires at the periphery.

As shown in the figure, the circumferential pressure (f_l) is provided by the 3DPM embedded with steel wires at the periphery:

$$f_l = f_{l,3DP} + f_{l,sw} \tag{2}$$

Due to the low reinforcement ratio of the steel wire, $f_{l,3DP}$ can be calculated as follows[36]:

$$f_{l,3DP} = k_h \frac{2t\sigma_{h,3DP}}{D+t} \tag{3}$$

where k_h can be determined by Eq.(4) [39].

$$k_h = \frac{Ae}{A} = \frac{A - A_l}{A} = 1 - \frac{\sum_{i=1}^{n=4} (B-2r)^2/6}{A} = 1 - \frac{2(B-2r)^2}{3A} \tag{4}$$

Considering that the restraining effect of the embedded steel wire on the concrete is similar to the restraining effect of ordinary hoops, the effective coefficient of restraint in the vertical direction can be determined as Eq. (5) [39]:

$$k_v = \left(1 - \frac{s}{2B}\right)^2 \tag{5}$$

Therefore, the circumferential circumferential pressure provided by the helical wires ($f_{l,sw}$) can be expressed as follows [39]:

$$f_{l,s\omega} = k_h k_v \frac{2A_{sw}\sigma_{h,sw}}{Ds} \tag{6}$$

Finally, the total circumferential pressure f_l represents provided by the outer layer of 3DPM embedded in the wire, as follow:

$$f_l = k_h \frac{2t\sigma_{h,3DP}}{D+t} + k_h k_v \frac{2A_{sw}\sigma_{h,sw}}{Ds} \tag{7}$$

4.3. Stress-strain relationship of steel wire and 3DPM

In this experiment, the outer layer of 3D reinforced mortar was exposed to both axial compression and lateral tension. However, there is limited research on cementitious composites under multiaxial strain [36]. In this paper, the stress-strain model of ECC under biaxial tension-compression illustrated in Fig. 10 [32], is utilized to analyze the tensile stress-strain behavior of concrete confined by wire-reinforced 3DPM.

Since the material in this experiment is not mixed with fibers and the strength of the specimen decreases significantly after damage, only the elastic phase (the red part of the curve) is considered in the calculations in this paper. $\sigma_{h,3DP}$ can be expressed as Eq.(8) [36].

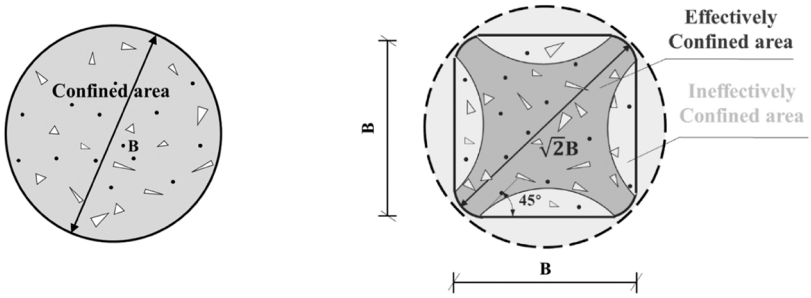

(a) General circular cross-section (b) Equivalent circular cross-section

Fig. 8. Constrained cross-section model.

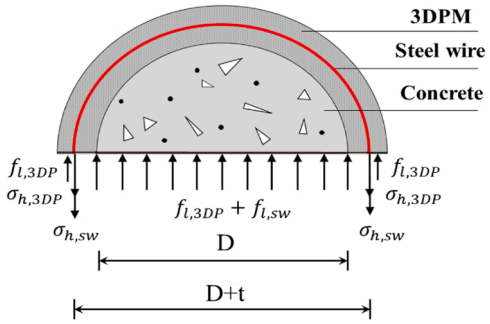

Fig. 9. Equivalent perimeter pressure.

$$\sigma_{h,3DP} = \begin{cases} \dfrac{E_{3DP}}{1-\mu^2}(\varepsilon_e + \mu\varepsilon_c) & ,\sigma_{h,3DP} < f_{cr} \\ f_{cr} & ,\sigma_{h,3DP} \geq f_{cr} and \sigma_{h,3DP} \geq 0.25\sigma_{3DP} \\ f_{cr}\dfrac{\varepsilon_s - \varepsilon_c}{\varepsilon_s - \varepsilon'_{cr}} & ,\sigma_{h,3DP} \geq f_{cr} and \sigma_{h,3DP} < 0.25\sigma_{3DP} \end{cases} \tag{8}$$

The axial compressive strain refers to the axial compressive stress of concrete. In addition, the axial compressive stress of 3DPM can be determined based on the ECC compression stress-strain model [36] as follows:

$$\sigma_{3DP} = \begin{cases} \left[1.1\left(\dfrac{\varepsilon_c}{\varepsilon_{ce}}\right) + 0.5\left(\dfrac{\varepsilon_c}{\varepsilon_{ce}}\right)^5 - 0.6\left(\dfrac{\varepsilon_c}{\varepsilon_{ce}}\right)^6\right]\sigma_{ce} & ,(0 \leq \dfrac{\varepsilon_c}{\varepsilon_{ce}} \leq 1) \\ \left[\dfrac{0.15\left(\frac{\varepsilon_c}{\varepsilon_{ce}}\right)^2}{1 - 2\left(\dfrac{\varepsilon_c}{\varepsilon_{ce}}\right) + 1.15(\frac{\varepsilon_c}{\varepsilon_{ce}})^2}\right]\sigma_{ce} & ,(\dfrac{\varepsilon_c}{\varepsilon_{ce}} \geq 1) \end{cases} \tag{9}$$

The reference research indicates that the σ_{ce} and ε_{ce} can be considered as $0.9f_{ce}$ (cubic compressive strength of 3DPM) and 0.005 [36]. Also, considering the thicker confining layer of 3DPM, the equivalent annular tensile strain in the equation (ε_e) can be obtained by the following equation[40]:

$$\varepsilon_e = \varepsilon_h\left[\frac{(1-2\mu) + (r_a/r_b)}{(1-2\mu) + (r_a/r_b)^2}\right] \tag{10}$$

where, the r_a and r_b are the inner and outer diameters of the printed paste, respectively, as shown in Fig. 11; ε_h represents the circumferential tensile strain of the concrete surface[37]:

$$\varepsilon_\theta = \varepsilon_h\left[\frac{(1-2\mu) + (r_a/r)^2}{(1-2\mu) + (r_a/r_b)^2}\right] \tag{11}$$

By setting values of r and ε_θ equal to r_b and the hoop tensile strain of 3DPM surface in the test, respectively.

The embedded steel wire within the outer mortar also contributes to the constraint. As the internal concrete is pressurized and

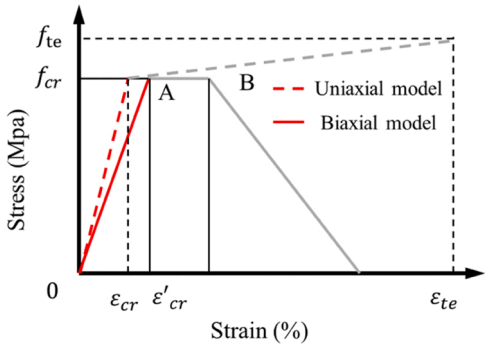

Fig. 10. Tensile stress-strain curve of 3DPM.

expands outward, the steel wire in the mortar experiences axial tension. The tensile stress of the steel wire can be calculated using a tensile stress-strain model [38]:

$$\frac{\sigma_{h,sw}}{f_y} = 3.33\frac{\varepsilon_{sw}}{\varepsilon_u} - 3.36\left(\frac{\varepsilon_{sw}}{\varepsilon_u}\right)^2 + 1.33\left(\frac{\varepsilon_{sw}}{\varepsilon_u}\right)^3 \tag{12}$$

Stress-strain relationship of concrete under constant circumferential confining stress according to [40]:

$$\frac{\sigma_c}{f_{cc}} = \frac{(\varepsilon_c/\varepsilon_{cc})\gamma}{\gamma - 1 + (\varepsilon_c/\varepsilon_{cc})^{\gamma}} \tag{13}$$

$$\gamma = \frac{E_c}{E_c - f_{cc}/\varepsilon_{cc}} \tag{14}$$

The peak axial stress and the corresponding compressive strain are calculated as follows [41]:

$$f_{cc} = f_{co} + 6.7f_l^{0.83} \tag{15}$$

$$\frac{\varepsilon_{cc}}{\varepsilon_{co}} = 1 + 5\left(\frac{f_{cc}}{f_{co}} - 1\right) \tag{16}$$

The tensile strain state and the circumferential tensile strain in the annular direction of 3DPM are not uniformly distributed around the perimeter of the extended section:

$$\frac{\frac{\varepsilon_c}{\varepsilon_{co}}}{\left[\left(1+3\frac{f_l}{f_{co}}\right)\left(1-0.07\frac{-\varepsilon_e}{\varepsilon_{ce}}\right)\right]} = 0.85\left\{\left[1+0.75\left(\frac{-\varepsilon_l}{\varepsilon_{co}}\right)\right]^{0.7} - e^{\left[-7\left(\frac{-\varepsilon_l}{\varepsilon_{co}}\right)\right]}\right\} \tag{17}$$

The axial compressive stresses in the concrete core and 3DPM were calculated using the previously mentioned equations. This calculation assumes the initial equivalent annular tensile strains and circumferential pressures, ensuring that the results meet the specified error limits for the provided values. The calculated results are presented in the table below:

Through iterative selection of assumed parameters, the initial equivalent circumferential strain of the circular cross-section specimen in the table is set to 0.005, and the radius of the fillet is 0. In the square specimen, the initial equivalent circumferential strain is set to 0.005. The radius of the fillet is 12.5 mm, and the remaining calculation method follows the approach for determining the equivalent circular cross-section. From the table, it is evident that the circumferential pressure around the annular specimen is higher than that around the circular specimen when the same type of steel wire is used.

Finally, the compressive load-strain relationship of wire-reinforced 3DPM confined concrete has been determined:

$$F = \sigma_c A_c + \sigma_{3DP} A_{3DP} \tag{18}$$

Where F is the load applied to the confined concrete column, A_c and A_{3DP} are the cross-sectional areas of the inner concrete layer, and the outer 3DPM layer. When calculating a square section, the shape of the section is equivalent to a circular section, and there is an ineffectively constraint area under compressive stress. So, this article adjusts the inner layer concrete area by 1.05 times and the outer layer mortar by 0.5 times based on the ratio of actual area to calculated area during the calculation process.

4.4. Procedures of the proposed model

Fig. 12 shows the procedures of the analytic model:

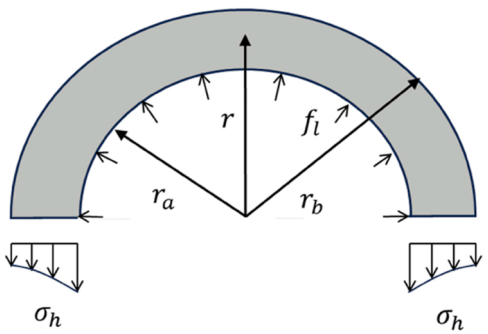

Fig. 11. Circumferential forces.

1) by assuming a confining pressure ($f_{l,a}$) for a given initial equivalent hoop tensile strain (ε_e) of 3DPM, calculating the corresponding axial compressive strain (ε_c) of the concrete core by Eq.(17);
2) determining the hoop tensile stress ($\varepsilon_{h,3DP}$) of 3DPM and the hoop tensile stress ($\varepsilon_{h,sw}$) of steel wire according to the tensile stress–strain models of 3DPM expressed by Eqs. (8) and (12), respectively
3) comparing the confining pressure (f_l) calculated by Eq. (7) with the assumed confining pressure ($f_{l,a}$);
4) calculating the peak axial compressive stress (f_{cc}) and its corresponding compressive strain (ε_{cc}) of confined concrete under a constant confining pressure (f_l) by Eqs. (15) and (16);
5) obtaining the axial compressive stress (σ_c) of concrete core and the axial compressive stress (σ_{3DP}) of 3DPM by using Eqs. (9) and (13);
6) 6) repeat steps 1–5 by increasing the equivalent hoop tensile strain (ε_θ) until the compressive strain of concrete core (ε_c) reaches the compressive strain corresponding to the ultimate load (ε_s) of confined concrete.

The calculation results that follow are derived from the aforementioned parameters:

Table 4 presents the calculated, tested, and calculated-compressive values for each type of concrete column. It is evident that the calculated compressive values of square columns are slightly lower than the compressive test values. The addition of fine steel wires results in lower tested and calculated values compared to the unwired specimen, while the addition of medium steel wires leads to higher values than the unwired specimen. The compressive values calculated for the cylinders were generally lower than the test values, except for the specimen with the addition of fine steel wires. The calculated results increased as the diameter of the wires increased. The errors in the calculated values compared to the tested values are lower than 15 %, except for the fine-wire columns. The above comparisons indicate that the proposed analytical model can reasonably estimate the compressive stress-strain relationship of the restrained concrete by the steel wire 3D-printed mortar. However, it is important to note that for more accurate prediction of the compressive properties of concrete, further studies are required on the stress-strain relationship of 3D printed mortar under tensile-compressive stress states.

5. Conclusion

This study investigated the compressive performance and damage mechanism of wire-reinforced 3DPM-constrained concrete columns under uniaxial compression. The effects of the section shape and the steel wire diameter were considered. A compressive stress-strain analytical model was established to characterize the constrained concrete columns. The main conclusions are presented below.

(1) The trend of stress-strain curves in both S and C-series are similar, which is approximated to be divided into three stages. In the two series of specimens, the effect of steel wires on the ultimate compressive capacity was different. In the S-series, the compressive strength behaves in the order of S-M>S-N>S-F. In C-series, the peak stresses of the three specimens C-N, C-M, and C-T were approximated the same, the specimen C-F behaved with the lowest stress.
(2) DIC analysis found that the square columns are particularly susceptible to developing cracks at the corners of the column ends and extend downward. In comparison to the specimens S-N and S-F, the number of cracks decreased and the cracks became narrower in the specimens S-M. Combined with the effect of steel wire on the compressive strength, an appropriate increase in the reinforcement ratio of the 3DPM can be beneficial for enhancing the confinement capacity in S-series columns.
(3) The number of cracks and cracking width of C-series specimens are higher than those of S-series. Compared to the specimens without steel wires, cracks in specimens C-M appear later, and there are more and finer cracks inside the specimens before failure. The cracking widths of both C-M and S-M are the lowest in both series, which proves once again the positive effect of the appropriate reinforcement ratio on the load-bearing capacity of confined columns.
(4) Based on the uniaxial compression model of ECC confined concrete, this paper proposes a preliminary compressive stress-strain analytical model for wire-reinforced 3DPM confined concrete. Where, the calculated/tested values for the S-series are in the range of 0.9–1.0, the value for the C series in the range of 0.9–1.2. The specimens with fine steel wires in both series show the lowest strengths, which result in large deviations between the calculated and tested values.

This paper investigates the compressive performance of wire-reinforced 3DPM-constrained concrete columns, which clarifies the effectiveness in the improvement of compressive performance by the reinforced 3DPM. Further research on the design method of the appropriate reinforcement rate of steel wire and the establishment of a more perfect theoretical analysis model of restrained short columns will play an important significance for the future application of 3DPM in engineering.

CRediT authorship contribution statement

Wengui Li: Investigation. **Feng Pan:** Investigation. **Chang Sun:** Writing – review & editing, Supervision, Resources, Project administration, Methodology, Funding acquisition, Formal analysis, Conceptualization. **Jiawang Li:** Writing – original draft, Visualization, Investigation. **Qiong Liu:** Writing – review & editing, Supervision, Resources, Conceptualization. **Kailun Chen:** Investigation.

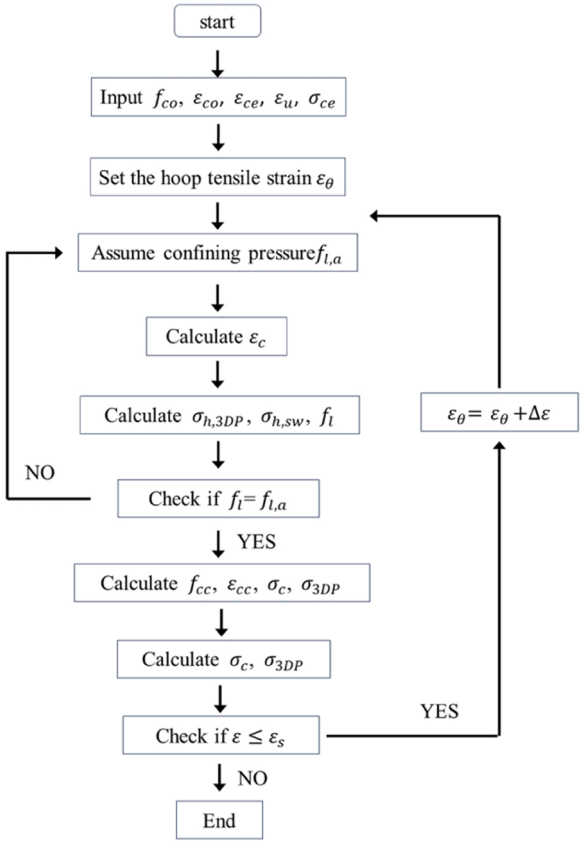

Fig. 12. Steps of the analytical model.

Table 4
Comparison of predicted and actual values (unit: MPa).

Specimen	S-N	S-F	S-M	C-N	C-F	C-M	C-T
Test	25.38	20.95	35.76	36.90	26.94	36.56	34.12
Cal	25.11	20.41	32.62	32.67	32.70	33.49	34.05
Cal/Test	0.990	0.974	0.912	0.885	1.214	0.916	0.998

Declaration of Competing Interest

The authors declare that they have no known competing financial interests or personal relationships that could have appeared to influence the work reported in this paper.

Data availability

Data will be made available on request.

Acknowledgments

The authors sincerely acknowledge the financial support from the Shanghai Rising-Star Program, grant number 22QC1400900.

References

[1] D. Dey, D. Srinivas, B. Panda, P. Suraneni, T.G. Sitharam, Use of industrial waste materials for 3D printing of sustainable concrete: a review, J. Clean. Prod. 340 (2022) 130749, https://doi.org/10.1016/j.jclepro.2022.130749.
[2] B. Structures, Research progress on low carbon characters of concrete 3D-printing based construction, (2023).
[3] J.G. Yue, D.E. Beskos, C. Feng, K. Wu, Hardened fracture characteristics of printed concrete using acoustic emission monitoring technique, Constr. Build. Mater. 361 (2022) 129684, https://doi.org/10.1016/j.conbuildmat.2022.129684.

[4] A. Ramesh, P. Rajeev, J. Sanjayan, Bond-slip behaviour of textile-reinforcement in 3D printed concrete, J. Build. Eng. 86 (2024) 108873, https://doi.org/10.1016/j.jobe.2024.108873.
[5] X. Huang, W. Yang, F. Song, J. Zou, Study on the mechanical properties of 3D printing concrete layers and the mechanism of influence of printing parameters, Constr. Build. Mater. 335 (2022) 127496, https://doi.org/10.1016/j.conbuildmat.2022.127496.
[6] M. Farahbakhsh, Z.K. Rybkowski, U. Zakira, N. Kalantar, I. Onifade, Impact of robotic 3D printing process parameters on interlayer bond strength, Autom. Constr. 142 (2022) 104478, https://doi.org/10.1016/j.autcon.2022.104478.
[7] X. Liu, B. Sun, The influence of interface on the structural stability in 3D concrete printing processes, Addit. Manuf. 48 (2021) 102456, https://doi.org/10.1016/j.addma.2021.102456.
[8] Y. Yang, C. Wu, Z. Liu, H. Zhang, 3D-printing ultra-high performance fiber-reinforced concrete under triaxial confining loads, Addit. Manuf. 50 (2022) 102568, https://doi.org/10.1016/j.addma.2021.102568.
[9] W. Zhou, W. McGee, H. Zhu, H.S. Gökçe, V.C. Li, Time-dependent fresh properties characterization of 3D printing engineered cementitious composites (3DP-ECC): on the evaluation of buildability, Cem. Concr. Compos. 133 (2022), https://doi.org/10.1016/j.cemconcomp.2022.104704.
[10] H. Noorvand, B. Mobasher, S. Underwood, K. Kaloush, Development of an analytical framework for evaluation of critical fiber length in asphalt concrete with a fiber pullout test, Constr. Build. Mater. 360 (2022) 129561, https://doi.org/10.1016/j.conbuildmat.2022.129561.
[11] V. Sergis, C.M. Ouellet-Plamondon, D-optimal design of experiments applied to 3D high-performance concrete printing mix design, Mater. Des. 218 (2022) 110681, https://doi.org/10.1016/j.matdes.2022.110681.
[12] J. Katzer, A. Skoratko, Using 3D printed formworks for the creation of steel fibre reinforced concrete-plastic columns, Constr. Build. Mater. 337 (2022) 127586, https://doi.org/10.1016/j.conbuildmat.2022.127586.
[13] K. Yu, L. Li, J. Yu, J. Xiao, J. Ye, Y. Wang, Feasibility of using ultra-high ductility cementitious composites for concrete structures without steel rebar, Eng. Struct. 170 (2018) 11–20, https://doi.org/10.1016/j.engstruct.2018.05.037.
[14] T. Marchment, J. Sanjayan, Bond properties of reinforcing bar penetrations in 3D concrete printing, Autom. Constr. 120 (2020) 103394, https://doi.org/10.1016/j.autcon.2020.103394.
[15] Y. Chen, W. Zhang, Y. Zhang, Y. Zhang, C. Liu, D. Wang, Z. Liu, G. Liu, B. Pang, L. Yang, 3D Printed concrete with coarse aggregates: built-in-stirrup permanent concrete formwork for reinforced columns, J. Build. Eng. 70 (2023) 106362, https://doi.org/10.1016/j.jobe.2023.106362.
[16] A. Aramburu, I. Calderon-Uriszar-Aldaca, I. Puente, Bonding strength of steel rebars perpendicular to the hardened 3D-printed concrete layers, Constr. Build. Mater. 340 (2022) 127827, https://doi.org/10.1016/j.conbuildmat.2022.127827.
[17] M. Hojati, A.M. Memari, M. Zahabi, Z. Wu, Z. Li, K. Park, S. Nazarian, J.P. Duarte, Barbed-wire reinforcement for 3D concrete printing, Autom. Constr. 141 (2022), https://doi.org/10.1016/j.autcon.2022.104438.
[18] J. Xiao, Z. Chen, T. Ding, S. Zou, Bending behaviour of steel cable reinforced 3D printed concrete in the direction perpendicular to the interfaces, Cem. Concr. Compos. 125 (2022) 104313, https://doi.org/10.1016/j.cemconcomp.2021.104313.
[19] Z. Li, L. Wang, G. Ma, Mechanical improvement of continuous steel microcable reinforced geopolymer composites for 3D printing subjected to different loading conditions, Compos. Part B Eng. 187 (2020) 107796, https://doi.org/10.1016/j.compositesb.2020.107796.
[20] V. Mechtcherine, J. Grafe, V.N. Nerella, E. Spaniol, M. Hertel, U. Füssel, 3D-printed steel reinforcement for digital concrete construction – manufacture, mechanical properties and bond behaviour, Constr. Build. Mater. 179 (2018) 125–137, https://doi.org/10.1016/j.conbuildmat.2018.05.202.
[21] M.X. Xiong, Z. Xu, G.M. Chen, Z.H. Lan, FRP-confined steel-reinforced recycled aggregate concrete columns: concept and behaviour under axial compression, Compos. Struct. 246 (2020), https://doi.org/10.1016/j.compstruct.2020.112408.
[22] Y. Ding, Z. Zhou, Y. Wei, Y. Huang, H. Tian, Axial compressive behavior of ultra-high performance concrete confined by high-strength transverse reinforcements, Constr. Build. Mater. 324 (2022) 126518, https://doi.org/10.1016/j.conbuildmat.2022.126518.
[23] Z. Chen, W. Qin, Y. Liang, J. Zhou, Axial compressive performance of seawater sea sand concrete-filled CFRP-stainless steel tube short columns, Constr. Build. Mater. 369 (2023) 130501, https://doi.org/10.1016/j.conbuildmat.2023.130501.
[24] Z. Yang, C. Xu, G. Li, Behavior of GFRP tube confined hollow high-strength concrete short columns under axial compression, Structures 61 (2024) 106017, https://doi.org/10.1016/j.istruc.2024.106017.
[25] G.M. Chen, Z.H. Lan, M.X. Xiong, Z. Xu, Compressive behavior of FRP-confined steel-reinforced high strength concrete columns, Eng. Struct. 220 (2020), https://doi.org/10.1016/j.engstruct.2020.110990.
[26] F. Yuan, J. Song, Y. Wu, Effect of compression casting method on the axial compressive behavior of FRP-confined seawater sea-sand concrete columns, Eng. Struct. 290 (2023) 116311, https://doi.org/10.1016/j.engstruct.2023.116311.
[27] Z. Xiong, Y. Zeng, L.G. Li, A.K.H. Kwan, S.H. He, Experimental study on the effects of glass fibres and expansive agent on the bond behaviour of glass/basalt FRP bars in seawater sea-sand concrete, Constr. Build. Mater. 274 (2021), https://doi.org/10.1016/j.conbuildmat.2020.122100.
[28] H. Zhao, Axial compressive behaviour of concrete strengthened with steel rings, wire mesh and modified high strength mortar (MHSM), Constr. Build. Mater. 250 (2020) 118938, https://doi.org/10.1016/j.conbuildmat.2020.118938.
[29] Z. Zhao, M. Chen, Y. Jin, L. Lu, L. Li, Rheology control towards 3D printed magnesium potassium phosphate cement composites, Compos. Part B Eng. 239 (2022) 109963, https://doi.org/10.1016/j.compositesb.2022.109963.
[30] B. Panda, S. Ruan, C. Unluer, M.J. Tan, Improving the 3D printability of high volume fly ash mixtures via the use of nano attapulgite clay, Compos. Part B Eng. 165 (2019) 75–83, https://doi.org/10.1016/j.compositesb.2018.11.109.
[31] C. Liu, R. Zhang, H. Liu, C. He, Y. Wang, Y. Wu, S. Liu, L. Song, F. Zuo, Analysis of the mechanical performance and damage mechanism for 3D printed concrete based on pore structure, Constr. Build. Mater. 314 (2022) 125572, https://doi.org/10.1016/j.conbuildmat.2021.125572.
[32] Y. Chen, J. Wei, H. Huang, W. Jin, Q. Yu, Application of 3D-DIC to characterize the effect of aggregate size and volume on non-uniform shrinkage strain distribution in concrete, Cem. Concr. Compos. 86 (2018) 178–189, https://doi.org/10.1016/j.cemconcomp.2017.11.005.
[33] Y. Wei, X. Wang, K. Li, L. Jin, J. Zhu, Behavior of confined concrete columns with HSSSWR meshes reinforced ECC jacket under uniaxial compression, Constr. Build. Mater. 342 (2022), https://doi.org/10.1016/j.conbuildmat.2022.127930.
[34] P. Li, Y. Chen, F. Yuan, Stress-strain behavior of ECC-GFRP spiral confined concrete cylinders, J. Build. Eng. 63 (2023) 105473, https://doi.org/10.1016/j.jobe.2022.105473.
[35] K. Le Nguyen, M.Q. Cao, X.H. Nguyen, S. Banihashemi, A. Si Larbi, Experimental and numerical investigation for confined concrete elements with fabric reinforced cementitious matrix (FRCM), Constr. Build. Mater. 382 (2023), https://doi.org/10.1016/j.conbuildmat.2023.131280.
[36] J.B. Mander, M.J.N. Priestley, R. Park, Modelo teórico esfuerzo-deformación para hormigón confinado, J. Struct. Eng. 114 (1989) 1804–1826.
[37] M.M. Karthik, J.B. Mander, S. Hurlebaus, Simulating behaviour of large reinforced concrete beam-column joints subject to ASR/DEF deterioration and influence of corrosion, Eng. Struct. 222 (2020) 111064, https://doi.org/10.1016/j.engstruct.2020.111064.
[38] T. Ozbakkaloglu, J.C. Lim, T. Vincent, FRP-confined concrete in circular sections: review and assessment of stress-strain models, Eng. Struct. 49 (2013) 1068–1088, https://doi.org/10.1016/j.engstruct.2012.06.010.
[39] Weikang Liu. Study on the compression and tensile properties and the constitutive model of ECC [D]. Zhengzhou University.
[40] J. Xie, Q. Fu, J.B. Yan, Compressive behaviour of stub concrete column strengthened with ultra-high performance concrete jacket, Constr. Build. Mater. 204 (2019) 643–658, https://doi.org/10.1016/j.conbuildmat.2019.01.220.
[41] X. Wang, G. Yang, W. Qian, K. Li, J. Zhu, Tensile behavior of high-strength stainless steel wire rope (HSSSWR)-reinforced ECC, Int. J. Concr. Struct. Mater. 15 (2021), https://doi.org/10.1186/s40069-021-00480-x.